Author(s): Andrea Parisi and Robin C. Ball

Article Title: Role of surface waves on the relation between crack speed and the work of fracture

Year of publication: 2002

Link to published article:
http://dx.doi.org/10.1103/PhysRevB.66.165432

Publisher statement: http://dx.doi.org/10.1103/PhysRevB.66.165432

Role of surface waves on the relation between crack speed and the work of fracture

Andrea Parisi and Robin C. Ball
Department of Physics, University of Warwick, Coventry CV4 7AL, United Kingdom
(Dated: February 1, 2008)

We show that the delivery of fracture work to the tip of an advancing planar crack is strongly reduced by surface phonon emission, leading to forbidden ranges of crack speed. The emission can be interpreted through dispersion of the group velocity, and Rayleigh and Love branches contribute as well as other high frequency branches of the surface wave dispersion relations. We also show that the energy release rate which enters the Griffith criterion for the crack advance can be described as the product of the continuum solution with a function that only depends on the lattice geometry and describes the lattice influence on the phonon emission. Simulations are performed using a new finite element model for simulating elasticity and fractures. The model, built to allow fast and very large three-dimensional simulations, is applied to the simplified case of two dimensional samples.

PACS numbers: 62.20.Mk, 62.30.+d, 02.70.Dh

I. INTRODUCTION

It is well known that fracture propagation is strongly governed by properties of the surface created. The classical Griffith criterion requires that for a crack to propagate all the elastic energy supplied to the crack tip must at least match the work of surface creation. Crack speed is more complicated: one needs to understand the energetics of mechanisms in competition with surface work, and in this paper we focus on phonon emission.

Phonon emission from the crack tip involves both bulk and surface waves. In the continuum limit these waves are dispersionless and emission is only expected when the crack speed matches any of the speeds v_l, v_t and v_R of longitudinal, transverse and Rayleigh (surface) waves. The Rayleigh speed being the lowest, it is often regarded as the ultimate theoretical limit for the speed of crack propagation. Real materials however have properties that do not match the continuum theory. One famous example of this is the existence of forbidden crack speeds, which was first explained by M. Marder *et al.*[3,4,5] taking into account the discrete nature of matter. Their qualitative explanation of the *velocity gap* where no crack can propagate in a periodic lattice at speeds lower than roughly 1/3 of the transverse waves speed, was related to lattice oscillations breaking bonds before the expected time compatible with the crack speed. This explanation involves the use of a "most stretched bond" breakage rule. Here we propose a more cautious but general view using an approach based on the phonon band structure and the energy release rate. The phonon band structure can lead to resonant emissions which influence the fraction of energy radiated from the crack tip. The existence of forbidden crack speeds then follows.

When dealing with dispersion relations the reference is usually to bulk waves or, in the case of surface waves, to the Rayleigh branch responsible for the Rayleigh speed. Geophysicists and researchers in earthquakes are also familiar with another kind of surface waves known as Love waves[6,7], polarized in the direction normal to that of propagation and parallel to the crack plane. Love waves only exist in the continuum limit when there is a gradation of elastic properties near the surface, pertinent to seismology but not usually considered in fracture mechanics. However, due to the discrete nature of matter at the atomic level dispersive media can also support Love and other wave branches so that they can enter fracture problems. It is natural to include the whole complexity of the surface dispersion relations in the description of the material to understand its role, and how and if this complexity can change the theoretical description of fracture dynamics.

The form of dispersion relations is the fingerprint of the discrete spatial organization of matter, beyond the continuum limit. In any kind of simulation it is necessary to deal with discretization in space. In molecular dynamic simulations[8,9,10] this corresponds to an atomistic description; in mesoscopic models as lattice-like[11,12,13,14] or finite element models[15,16,17], discretization has to be imposed in space in order to solve differential equations of the dynamics. This has an unavoidable effect on the dispersion relations that necessarily reflect the underlying lattice.

In this paper we present a new model developed to simulate an elastic continuum material using finite tetrahedral elements. Space is discretized on an fcc grid, and this is reflected in the dispersion relations of the simulated material. This feature could be considered a drawback, but can be exploited to model the influence of similar dispersions in real fcc structure materials. The simplicity of the model allows us an extensive understanding of both simulations and theory. The model, built to allow fast and very large three dimensional simulations, is used here in the simplified case of two dimensional samples, and phonon emission from the crack surface of planar cracks advancing at fixed speeds is analysed. An analysis of the influence of this emission on the crack dynamics is the aim of this work.

New and central to our approach is that we fix the crack properties (speed and shape) and measure some of the mechanical properties (stress, energy release rate). This can be done with success in two-dimensions and

gives new insight into the behaviour of some of these quantities. In particular, we show that the energy release rate is strongly influenced by the surface phonon emission at the crack tip through resonant emission at particular crack speeds, leading to the existence of narrow bands of permitted crack speed. We also show that the energy release rate which enters the Griffith criterion can be expressed as the continuum solution, multiplied by a microscopic function that only depends on the lattice geometry and that describes the lattice influence on the phonon emission.

The paper is organized as follows: in section II a full description of the model is provided, including the description of the bulk dispersion relations. In section III, a preliminary analysis of simulations of planar cracks at constant speed is given, and in section IV we relate the phonon emission to the dispersion relations of surface waves and we show the phenomenon of resonances. In section V we analyse how the energy release rate is influenced by the phonon emission and we derive the existence of bands of permitted crack speeds. Finally, conclusions and comparison with other works are given in section VI.

II. SIMULATION MODEL

The model is an application of the finite element method with the aim of simulating linear elasticity and fractures. In continuum linear elasticity[1] the Lagrangian has the form:

$$L = \int \left(\frac{\rho \dot{\mathbf{u}}^2}{2} - \frac{1}{2} \nabla \mathbf{u} : \overleftrightarrow{\sigma} \right) dV \tag{2.1}$$

where the stress tensor is given by[2]:

$$\overleftrightarrow{\sigma} = \lambda \mathrm{Tr}(\nabla \mathbf{u})\, \mathbb{1} + \mu [\nabla \mathbf{u} + (\nabla \mathbf{u})^T]. \tag{2.2}$$

The unsymmetrized strain tensor $\nabla \mathbf{u}$ from which the stress tensor, Lagrangian and hence equations of motion follow is central to our finite element scheme below.

The key driving features of the model are that the elastic response is as local as possible so that non-linearity and particularly rupture can be incorporated, whilst accidental soft modes are avoided and all mode frequencies are strictly upper bounded for stability of timestepping.

A. Definition of the elastodynamic model

To evaluate the unsymmetrized strain tensor, space is discretized using an fcc lattice and lattice points are connected using tetrahedral elements. Each element connects four points (see fig. 1), which is the minimum for a full local gradient calculation in three dimensions. On each lattice point, the displacement field $\mathbf{u}$ is defined, and the Lagrangian in its discretized form is given by:

$$L = \sum_v \frac{m \dot{\mathbf{u}}_v^2}{2} - \sum_t \frac{1}{2} \Omega' (\nabla \mathbf{u})_t : \overleftrightarrow{\sigma}_t \tag{2.3}$$

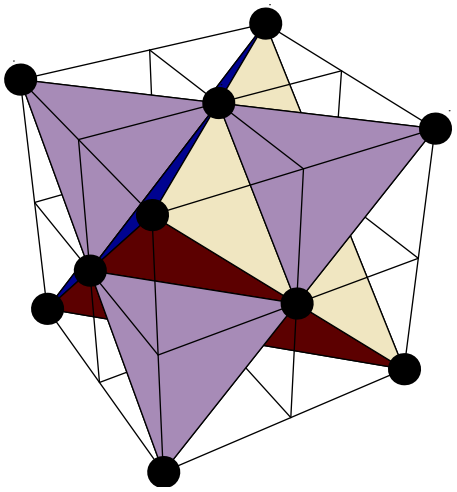

FIG. 1: Unit cell for the fcc lattice used in our simulations. This contains eight tetrahedra, each connecting four lattice sites. Displacement and momentum are defined on the sites, whilst strain and stress are defined on the tetrahedra.

where the v index spans over all lattice points and the t index spans all the tetrahedral elements. Ω' is the volume of the system per tetrahedron, 1/8 of the volume of the fcc conventional unit cell shown in fig. 1.

The stress tensor is evaluated at the center of each tetrahedron through (2.2), given the unsymmetrized strain tensor at the center of the t-th tetrahedron is:

$$(\nabla \mathbf{u})_t = \alpha \sum_v \mathbf{r}_{tv} \mathbf{u}_v \tag{2.4}$$

with the condition $\alpha \sum_v \mathbf{r}_{tv} \mathbf{r}_{tv} = \mathbb{1}$, where $\mathbf{r}_{tv}$ is the vector joining the center of the t-th tetrahedron with neighbouring vertex site v, and $\mathbf{u}_v$ is the displacement field on site v. Finally, the equation of motion takes then the form:

$$m \ddot{\mathbf{u}}_v = \mathbf{f}_v = -\alpha \Omega' \sum_t \mathbf{r}_{tv} \cdot \overleftrightarrow{\sigma}_t \tag{2.5}$$

where $\overleftrightarrow{\sigma}_t$ is the stress tensor of the tetrahedron.

B. Dispersion relations for bulk waves

The dispersion relations of our model are relatively straightforward to calculate. These confirm that in the long wavelength limit the continuum case is retrieved, and particularly that the use of tetrahedral elements avoids the presence of soft modes at the border of the Brillouin zone, a problem arising when using simple cubic schemes.

Introducing a spatial Fourier transform in equation (2.4), the gradient operator can be written as:

$$\mathrm{FT}[\nabla] = \alpha \sum_{\mathbf{r}_v} \mathbf{r}_v e^{i \mathbf{k} \cdot \mathbf{r}_v}. \tag{2.6}$$

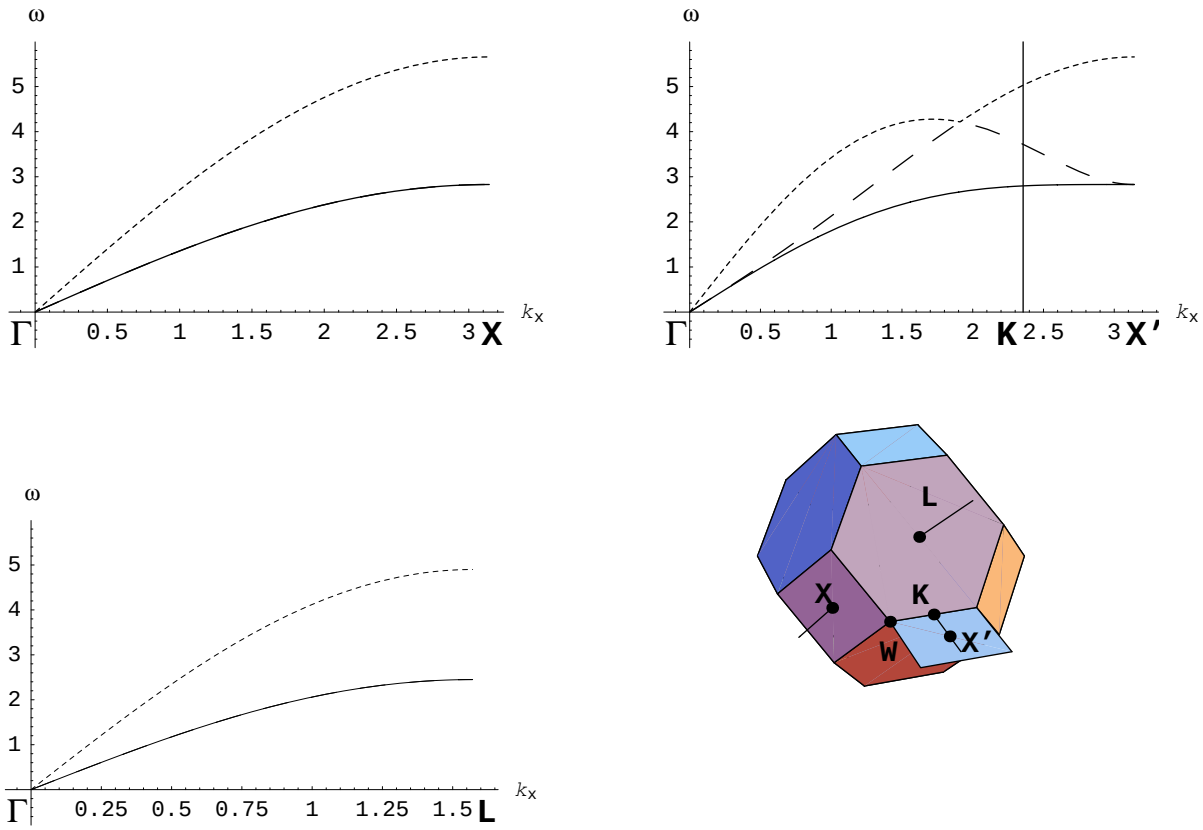

FIG. 2: Acoustic dispersion curves for the tetrahedron model along different directions in reciprocal space: there are no soft modes at the border of the Brillouin Zone. These plots are shown for Poisson's ratio $\nu = 1/3$ and using units where $a = 1$ for the side of the tetrahedral cell and $v_t = \sqrt{2}$ for the speed of transverse acoustic waves.

There are two kinds of tetrahedra (see fig. 1) which can be readily seen to be mirror images of each other, and their corresponding gradient operators are related, in the Fourier transform, by $\nabla_1 = -\nabla_2^*$. In terms of these eq. (2.5) can be expressed as:

$$m\ddot{\mathbf{u}} = \Omega' \Big[\nabla_2 \cdot \overleftrightarrow{\sigma}_1 + \nabla_1 \cdot \overleftrightarrow{\sigma}_2 \Big] \tag{2.7}$$

where

$$\overleftrightarrow{\sigma}_1 = \lambda \overleftrightarrow{I} \nabla_1 \cdot \mathbf{u} + \mu \Big[\nabla_1 \mathbf{u} + \mathbf{u} \nabla_1 \Big] \tag{2.8}$$

and $\overleftrightarrow{\sigma}_2$ is obtained by changing the index from 1 to 2 in eq. (2.8).

Equation (2.7) is therefore given, after Fourier transforming, by

$$m\omega^2 \mathbf{u_k} = \Omega' \Bigg\{ \mu \Big[\nabla \cdot \nabla^* + \nabla^* \cdot \nabla \Big] \mathbf{u_k} + \\ + (\lambda + \mu) \Big[\nabla \nabla^* + \nabla^* \nabla \Big] \cdot \mathbf{u_k} \Bigg\} \tag{2.9}$$

where $\nabla = \nabla_1 = -\nabla_2^*$. This equation can be solved exactly for eigenvalues (see appendix A), giving the results shown graphically in figure 2. The dispersion curves are well behaved, and reflect the underlying fcc structure: even if we are trying to simulate the continuum limit, dispersion relations are the image of the spatial structure of the underlying lattice. This cannot be avoided in our model just as in real materials.

The dispersion relations found vindicate the use of tetrahedral elements. Using a simpler cubic lattice and cubic finite elements leads to unphysical soft modes, where the frequency goes to zero whenever two of the three components of the **k** vector approach the border of the Brillouin zone. The use of tetrahedra removes this problem since there is no way to deform a tetrahedron giving a null contribution to the strain tensor, whilst alternative strategies involving less local spatial derivatives make fracture properties harder to implement and control.

The value of the maximum frequency is set by the longitudinal branch at the Brillouin Zone boundary. We will see in section II D that such a value remains an upper bound even when considering the finiteness of the sample or the presence of fractures. This value provides the minimum period of site motion.

Due to the significant role of surface waves in this paper, a study on their dispersion relations will be described

later in section IV.

C. Discretizing time

Time can be discretized by introducing a finite timestep h. The integration scheme used in our simulations is the *Leap-Frog* scheme[19], in which displacements $\mathbf{u}_v$ and momenta $\mathbf{p}_v$ are evaluated alternately at subsequent steps:

$$\begin{cases} \mathbf{u}_v(t) &= \mathbf{u}_v(t-2h) + 2h\dfrac{\mathbf{p}_v(t-h)}{m} \\ \mathbf{p}_v(t+h) &= \mathbf{p}_v(t-h) + 2h\mathbf{f}_v(t). \end{cases}$$

Fourier transforming these equations and comparing with the limit $h \to 0$ leads to the dispersion relation:

$$\sin^2(\omega h) = h^2\omega_0^2(\mathbf{k}) \tag{2.10}$$

where $\omega_0(\mathbf{k})$ is the value of the frequency of mode $\mathbf{k}$ in the continuous time ($h \to 0$) limit. From this equation it follows that we require $h\omega_0(\mathbf{k}) < \mathbf{1}$ for mode k to be stable in the discrete timestep simulations, and the global stability limit is

$$h < \Big[\max_{\mathbf{k}} \omega_0(\mathbf{k})\Big]^{-\mathbf{1}}.$$

It is interesting to apply this to the simplified case of one dimension. In this case the continuous time dispersion relations have the simple form

$$\omega_0^2(k) = \omega_{\max}^2 \sin^2\left(\frac{ka}{2}\right) \tag{2.11}$$

with: $\omega_{\max} = (2/a)\sqrt{(\lambda+2\mu)/\rho}$. Comparing (2.10) and (2.11), it is easy to observe that the stability limit for the timestep is $h = 1/\omega_{\max}$. Moreover, if we use exactly this value for the timestep, we obtain the linear dispersion relation $\omega = ck$ with $c = a\,\omega_{\max}/2$. Thus using the maximum allowed timestep, the relation between the frequency and the wave vector is the same as in continuum elasticity. This notable property is valid only in one dimension and is lost in two and three dimensions where the dispersion is more rich. Nevertheless, this property shows that having discretized space, it not necessarily an optimal approximation to the continuum to use a very small timestep as in standard Molecular Dynamics simulations.

In three dimensions $\omega_{\max}$ is given by the maximum frequency over the entire first Brillouin zone. Using the maximum allowed timestep dispersion relations are closer but not equivalent to the continuum limit.

The Leap-Frog scheme used here to discretize time is relatively robust with respect to energy conservation due to its time reveribility and symplectic properties.[20] There is an exactly conserved h-dependent hamiltonian H_h very close to the naïve one[20], with for example:

$$H_h \equiv \frac{1}{2}\Big(K_+ + K_-\Big) + U + \mathrm{O}(h^2) \tag{2.12}$$

where K_+ and K_- are the kinetic energies advanced and retarded by $\pm h$ relative to the timestep where the potential energy U is evaluated.

In these simulations the value chosen for the timestep has been $h = 0.1\ h_{\max}$. Using such timestep, dispersion relation are close to the continnum time dispersion relations. Some trial simulations with $h = 0.01\ h_{\max}$ have been performed showing no substantial difference with the results here reported.

D. Nonlinear elasticity and breakage

The model up to now has been described as a model for linear elasticity. However, since the link between the stress and the strain tensor is given exclusively through equation (2.2), we can easily generalize the equation to include any kind of elastic response as well as anisotropies. For instance:

$$\overleftrightarrow{\sigma} = \overleftrightarrow{\mathbf{f}}\Big(\nabla\mathbf{u} + (\nabla\mathbf{u})^T\Big) \tag{2.13}$$

where each tensor component f_{ij} represents any kind of nonlinear function. In this paper we study only the simpler scenario of linear elasticity augmented by breakage of tetrahedra corresponding to the advance of the crack. We brake tetrahedra by abruptly setting its elastic constants λ and μ to zero and it is the resulting recoil of the neighbouring sites which excites phonon emission.

Breaking tetrahedra does not compromise the maximum allowed timestep, because we can readily show that the maximum vibrational frequency cannot increase. To see this consider eq. (2.5) rewritten in the form

$$\rho\ddot{\mathbf{u}}_v = -\frac{\partial\mathcal{U}}{\partial\mathbf{u}_v}.$$

From (2.3), we clearly have $\sum_v \mathbf{u}_v \cdot \partial\mathcal{U}/\partial\mathbf{u}_v = 2\mathcal{U}$, where $\mathcal{U}$ is the total potential energy. Now consider a normal mode obeying:

$$\rho\omega^2\mathbf{u}_v = \frac{\partial\mathcal{U}}{\partial\mathbf{u}_v}$$

from which it follows that

$$\rho\omega^2 = \frac{2\mathcal{U}}{\sum_v |\mathbf{u}_v|^2}.$$

Breaking a tetrahedron removes strictly non-negative terms from the numerator of the right hand side, and this can only lower the maximum of ω.

III. SIMULATIONS OF PLANAR CRACKS AT CONSTANT SPEED

An advancing crack is simulated through the breaking of tetrahedra. To decide when to break we need a

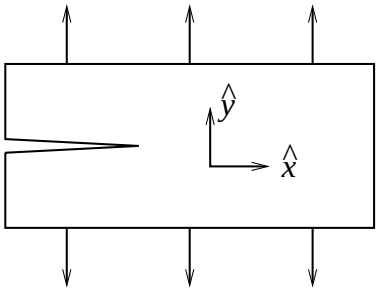

FIG. 3: Set-up for simulations. A fixed displacement is applied on the top and bottom boundaries, and the crack advances at constant speed up to the middle of the sample.

breakage rule. One possibility is to break tetrahedra as soon as they overcome some fracture criterion, for example a critical value of principal stress or elastic energy. In this work we instead follow a complementary approach, advancing a straight crack at constant speed and measuring the fracture criteria achieved such as work of fracture. This provides new insight into the relationship between energy release rate and crack speed, including any intervals of forbidden velocities.

For computational convenience we focussed on crack speeds commensurate with our timestep, that is

$$v_n = \frac{1}{2hn}$$

for $n = 1, 2, 3, \ldots$. Any desired crack speed can be obtained from this sequence by modest adjustment of the timestep h.

A. Stress field of advancing cracks

The model presented above is fully three dimensional. However for a strictly planar type-I crack, commensurate with our lattice, it is readily shown that the resulting dynamical solution is strictly planar with the displacement all in that plane. We have exploited this and shrunk our system to one fcc cell deep in the third dimension, with periodic boundary conditions.

In our simulations the Lamè coefficients are set so that the Poisson ratio is $\nu = 1/3$. The boundary conditions correspond to imposing fixed normal counter displacement at the top and bottom boundaries, i. e. $u_x = 0$, $u_y = \pm a$ at $y = \pm L/2$, and $\sigma_{xx} = \sigma_{xy} = 0$ on the right and left faces (see fig. 3). The initial condition is the static elastic solution, found by relaxing the lattice to its configuration of minimum energy by adding dissipation as discussed in appendix B. Because of the linearity of the equations, the magnitude of the imposed boundary displacement does not influence the results: for the following results the starting displacement is 1 % of the sample height. The advancing fracture is simulated until it reaches the middle of the sample, then a snapshot of the stress field is taken.

In figure 4.(a) the trace of the stress field for a typical simulation is shown: strong emission of surface waves is visible on the crack surface, as also shown in figure 4.(b). In particular, from this last figure it can be seen that the amplitude of these oscillations is smaller but of the same order of magnitude as the stress level at the crack tip.

B. Description of the basic phenomenon

When a crack is advancing new surface is being created, and waves are emitted both into the bulk and along the crack surface. In a system of reference comoving with the crack tip, the frequency ω' of emitted waves has to match the temporal frequencies with which lattice structure presents itself to the crack tip, leading to the selection rule:

$$\omega' = \omega - \mathbf{k}\cdot\mathbf{v} = \mathbf{g}\cdot\mathbf{v}$$

where $\mathbf{g}$ is any reciprocal lattice vector. This is equivalent to a simple matching of phase velocity:

$$\omega = \mathbf{k}\cdot\mathbf{v} \tag{3.1}$$

where the wave vector $\mathbf{k}$ is viewed in the extended zone scheme as sketched in fig. 5.

From a graphical point of view, a crack advancing at a given speed can be represented as a straight line in the (k_x, ω) plane, its slope given by the crack speed. The crack emits waves at the frequencies and wavelengths corresponding to the intercepts of this line with the dispersion relations (see fig. 5) in the extended zone scheme.

For some crack speeds condition (3.1) may be fulfilled not just for one $\mathbf{k}$ point, but over a neighbourhood of $\mathbf{k}$. This can readily be shown to reduce to:

$$\mathbf{v}_G = \frac{\partial\omega}{\partial\mathbf{k}} = \mathbf{v}. \tag{3.2}$$

This matching of phase velocity and group velocity (sketched as well in fig. 5) is the condition of resonant emission. We can expect for these crack speeds a sharp increase in the intensity of the phonon emission.

To take this discussion further we need to describe the dispersion relations of surface waves for our model, as detailed in the following section.

IV. DISPERSION RELATIONS FOR SURFACE WAVES

The description of the modes in which a lattice with an underlying fcc symmetry can vibrate is more complex than the one given by continuum elasticity. Frequency as a function of wave vector is no longer linear, and becomes periodic in the extended zone scheme. Moreover, new branches of surface wave appear besides the continuum Rayleigh branch. This richer band structure is crucial in understanding features on resonant phonon emission.

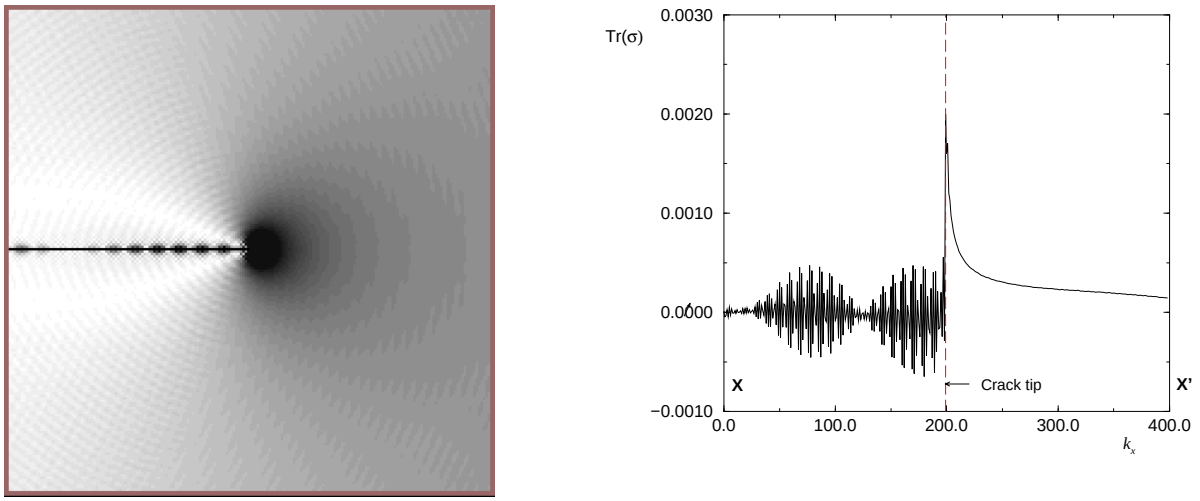

FIG. 4: (a) Absolute value of the trace of the stress field for a crack advancing at half of the transverse wave speed, with Poisson ratio $\nu = 1/3$. This is the central 200×200 region from a sample of 400×400 tetrahedra. Intensity spans from white (zero) to black (highest values). (b) Trace of the stress field measured along the fracture plane, through the crack tip whose singularity is clearly visible, and onwards ahead of the crack tip.

A. Theoretical surface dispersion relations

Due to the simplicity of the model it is not difficult to evaluate the dispersion relations of its surface waves. These are solutions of $\omega^2 \mathbf{u_k} + \nabla \cdot \overleftrightarrow{\sigma} = 0$ with boundary condition $\overleftrightarrow{\sigma} \cdot \mathbf{n} = 0$, where $\mathbf{n}$ is a unit vector normal to the surface. Solutions are linear combination of bulk modes characterized by the same frequency ω and surface wave vector components, and different complex $\mathbf{k} \cdot \mathbf{n}$ that give decay towards the interior of the sample.

Calculations of the surface modes are reported in appendix C. Results are shown in fig. 6.(a).

The figure shows quite a rich diagram which includes the Love branch and some high-frequency branches. It is clear that all the branches could take part in the process of phonon emission.

B. Direct measurement of surface waves

The dispersion relations can be directly measured by exciting the top free surface of a simulated elastic sample. Sites of the top face are displaced according to one specified wave vector k_x. The surface is let free to oscillate and the frequencies of the corresponding excited modes are measured. Changing the k_x vector at $k_z = 0$, the entire first Brillouin zone can be spanned and a direct measurement of the dispersion of surface waves can be obtained. Results are shown in figure 6.(b).

It is evident that all the surface excitation is associated with the theoretical branches. No emission corresponding to the Love branch is visible due to its polarization perpendicular to our two dimensional plane. We have not identified the reason why no emission is observed corresponding to the R_{IV} branch.

Our measurements do show continuation of the theoretical branches beyond their end points. We have verified from calculations of appendix C that these continuations correspond to frequencies with a small imaginary part.

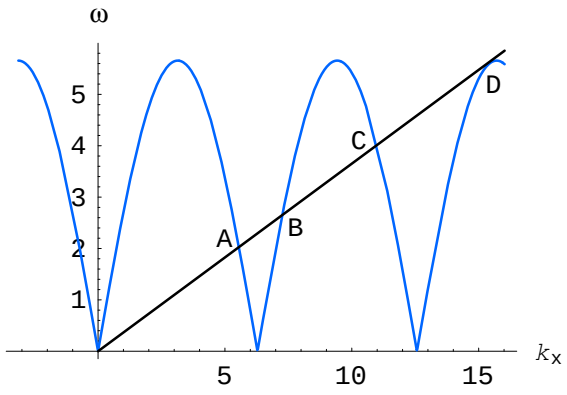

FIG. 5: Schematic description of the basic matching phenomena. A crack advancing at some speed v matches wave phase velocity at points A, B, C and D, so that corresponding phonons can be emitted from the crack tip. The figure shows the special case in which there is a *resonant* match at D: the crack speed also matches the wave's group velocity which should lead to strong emission.

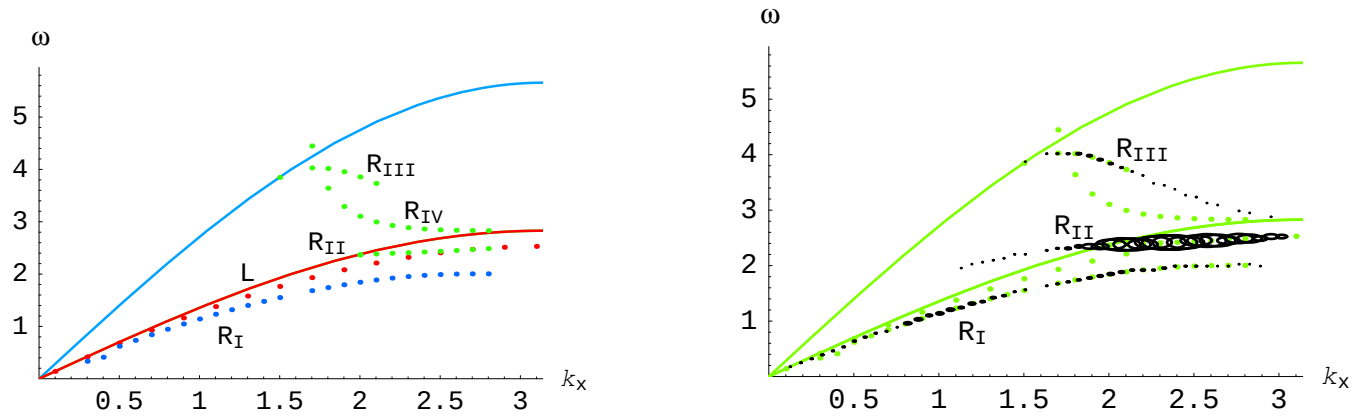

FIG. 6: (a) Points represent theoretical dispersion relations for surface waves in the first Brillouin zone, for our model with a $(0, 1)$ surface normal and $\nu = 1/3$, with units as in figure 2. Lines show the dispersion relations for bulk modes. All surface modes have $\mathrm{Im}(k_y) > 0$ to be damped for $y \to \infty$, and $k_z = 0$ corresponding to the two dimensional constraint in our simulations. The Rayleigh and Love branches are labelled as $\mathrm{R_I}$ and L. The other high frequency branches are not interpretable in the continuum limit. (b) Dispersion relations measured by excitation of a free surface, compared with the theoretical branches. More than one frequency can be excited for a given k_x. The size of circles reflects the intensity of the signals. Only three of the five branches are excited: the Love branch is not visible due to its polarization, however it is not clear the reason of the lack of evidence of the $\mathrm{R_{IV}}$ branch.

C. Emission from advancing cracks

Let us consider a snapshot at time t of the crack surface. Depending on the crack speed, some of the vibrational modes will be excited. Through a Fourier transform of the surface profile the excited k-vector can be obtained. Assuming that eq. (3.1) applies we can compare observed values of k_x at crack speed v with k_x versus ω/k_x from the theoretical dispersion relations. The one delicate point is that k_x is indeterminate up to multiples of a reciprocal lattice vector g. Figure 7 shows the agreement between measured emission and the theoretical curves, with assignment of multiples of g to the measured k_x as the only element of fitting.

D. Resonances

Resonances appear as soon as eq.(3.2) is fulfilled: this matching of phase velocity and group velocity can lead to resonant emission as sketched in fig. 5. Plotting the phase velocity ω/k_x versus k_x, the resonant condition is equivalent to a plateau in ω/k_x. Predicted resonances can therefore be easily read from our computed dispersion relations as shown in fig. 8. Due to the periodic band structure there is an infinite number of possible resonances corresponding to the infinite number of Brillouin zones. However we observe (not surprisingly) that signal corresponding to resonances in higher Brillouin zones is weak, so our discussion in this paper focuses on the first two Brillouin zones only.

The presence of resonances can be verified by analysing the total intensity of emitted waves as a function of crack speed. Figure 9 shows the total wave intensity integrated over just the crack surface, whilst the discussion of the full radiated wave power will be given in section V.

Corresponding to the speeds where resonances are expected there is an effective peak in the wave intensity. These peaks are slightly shifted towards lower speeds, which can be interpreted in terms of the concavity of dispersion relations at the resonance. When the crack advances at a speed slightly below the resonance, more modes can be excited, giving a maximum in intensity slightly shifted. The abrupt drop of intensity at higher

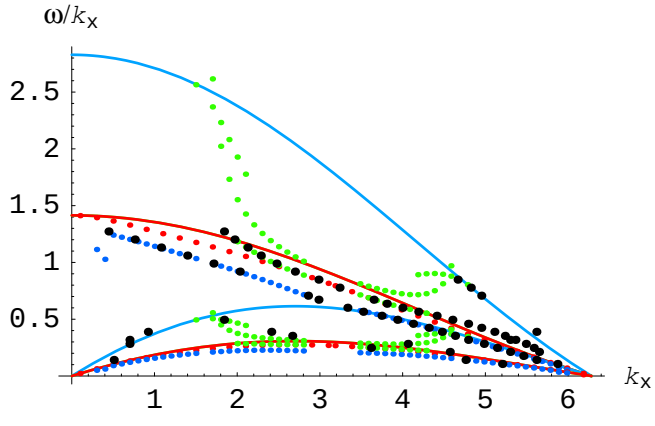

FIG. 7: In this plot crack speeds correspond to horizontal lines. Black dots correspond to the emission measured from the crack surface. For simplicity only emission from the first and second Brillouin zone (folded back into the first zone) has been reported. All dots lay on the theoretical dispersion relations or on their extensions in the second Brillouin zone.

crack speeds (approaching the Rayleigh speed) appears to result from the fact that the penetration length of such waves is of order their wavelength, and this in turn becomes of the order of the sample size as the Rayleigh speed is approached. At high speeds, the total intensity of surface waves cannot be retrieved by analysing just the crack profile.

V. ENERGY RELEASE RATE

The presence of resonances suggests that an effect on the crack dynamics has to be expected. We will now show how the most commonly and relevant measured quantity of crack dynamics, namely the *energy release rate*, is affected by this phenomenon.

In the simulations here reported, a planar crack is left to advance at constant speed from a short starting notch. At early times the crack is almost equivalent to a crack advancing in an unbounded medium, since the sample boundaries are distant from the crack tip. When the crack becomes large compared to the linear dimensions of the sample the crack starts to "feel" the presence of the boundaries and the correct description is that of a crack advancing in a strip. In the continuum and steady limit the short crack regime is characterized by a linear

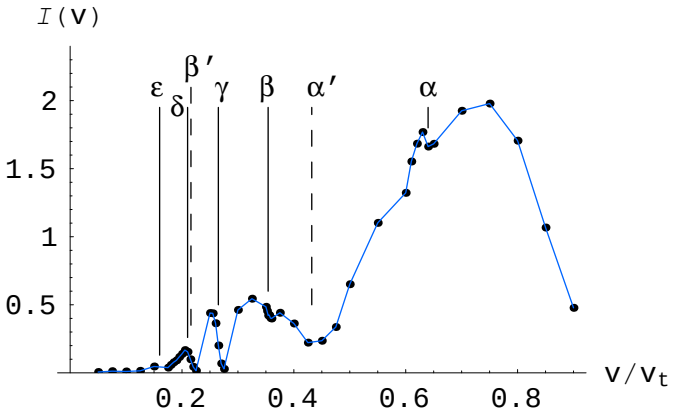

FIG. 9: The total wave intensity integrated over the fracture surface, as a function of crack speed. Peaks in the emission correspond to the resonances shown in figure 8, as indicated by vertical lines. A systematic shift towards the lower crack speeds is visible and is related to the convexity of the dispersion relations (see text). These results were obtained from simulations of samples of 800 × 800 tetrahedra.

increase of the energy release rate G with time, whilst in the long crack regime the G function is time-independent. Both regimes are sensitive to the crack speed.

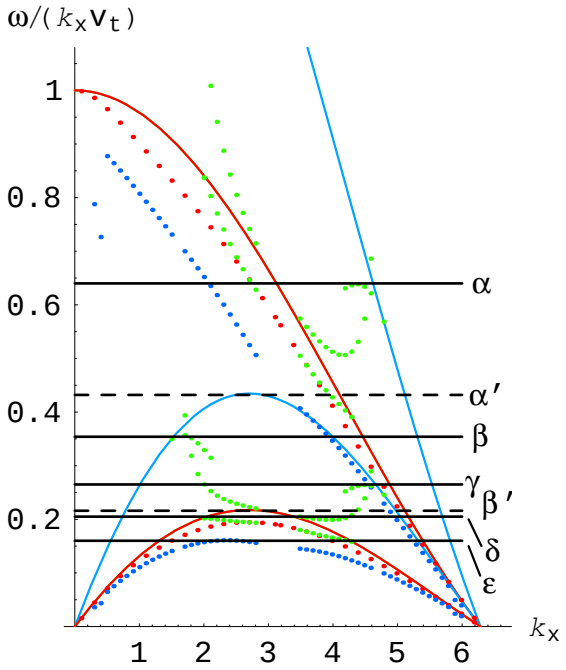

FIG. 8: The theoretical phase velocity ω/k_x versus k_x, with horizontal lines showing where resonant phonon emission can be expected. The lines show resonances due to the first and the second Brillouin zone only. Dashed lines correspond to resonances due to bulk dispersion relations.

1. *Energy release rate in a discrete sample*

The discrete nature of matter is reflected in the dependence of the energy release rate G on crack speed. We can describe the macroscopic energy release rate per unit distance of crack advance G_M as the sum of two contributions:

$$G_M(v,t) = G_{\rm br}(v,t) + G_{\rm ph}(v,t). \qquad (5.1)$$

$G_M(v,t)$ is the solution of the continuum limit which governs the macroscopic delivery of energy towards the crack tip, for which we have theoretical expressions available. $G_{\rm br}(v,t)$ and $G_{\rm ph}(v,t)$ are respectively the breakage energy release rate and the phonon energy release rate. Our strategy below is to directly measure the breakage energy release rate from the potential energy lost when tetrahedra are broken.

The macroscopic energy release rate $G_M(v,t)$ is largely determined by the macroscopic conditions and the length of the crack. In the long crack limit in the case of a strip of height $2l$ and fixed displacement δ at each boundary, the macroscopic energy release rate corresponds to the amount of elastic energy stored far ahead of the crack tip[2,18]. From eq.(2.2) the stress field ahead of the crack tip has

$$\sigma_{yy} = (\lambda + 2\mu)\epsilon \qquad (5.2)$$

where $\epsilon = \delta/l$ is the imposed strain. Hence the time

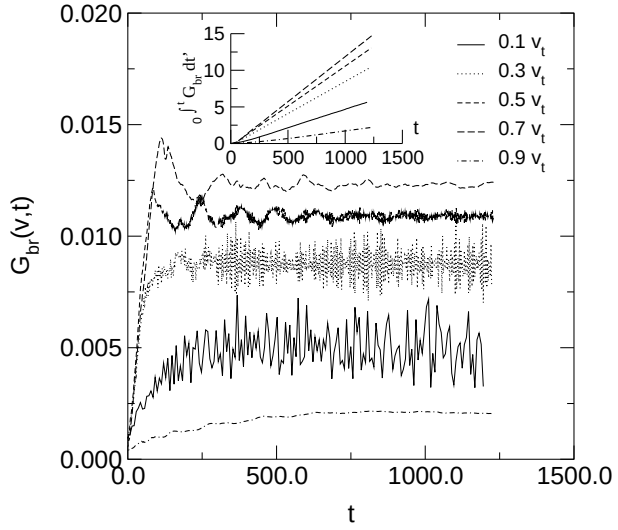

FIG. 10: The measured energy delivered into bond breaking per unit length of crack, as a function of time for different crack speeds. From these data we measured the early time slopes $G'_{\rm br}(v,0)$ corresponding to the short crack regime and (from the slope of the time integrated plots inset) the long crack plateau values $G_{\rm br}(v)$. The (non-trivial) sequence of the curves is more readily appreciated from fig. 11.

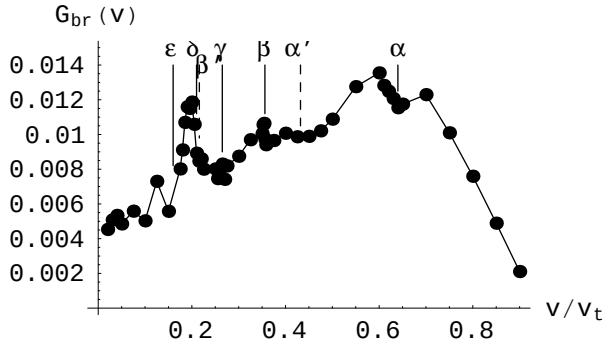

FIG. 11: Dependence of breakage energy release rate on crack speed in the long crack regime. Crack propagation with a steady speed should only be stable where this function is decreasing. Vertical lines show the theoretical position of resonant surface wave emission: the two dashed lines correspond to resonant bulk wave emission. The figure equivalently shows the behaviour of the efficiency $E(v)$ with the crack speed, as for long cracks and fixed grip conditions the two are strictly proportional.

independent macroscopic energy release rate is:

$$G_M^\infty = (\lambda + 2\mu)\epsilon^2 l \tag{5.3}$$

independent of the crack speed v.

The translation of the Griffith criterion in the discrete case is that the crack will advance as soon as the energy stored in the tetrahedron to break, $G_{\rm br}$, is greater than a threshold value connected with the toughness of the material. The behaviour of $G_{\rm br}$ with the crack speed is therefore crucial for understanding the crack dynamics.

The breakage energy release rate clearly depends on the external macroscopic conditions as well as the discreteness of the model. However it can be expressed as:

$$G_{\rm br}(v,t) = E(v)\, G_M(v,t) \tag{5.4}$$

where we have introduced the *efficiency* $E(v)$. In the long crack limit for the fixed grip set-up used in our simulations this gives $G_{\rm br}(v,t) = E(v)\, G_M^\infty$ where the efficiency is the sole source of velocity dependence. The effect of local discreteness thus separates from the effect of macroscopic external conditions: all the dependence on the crack speed is hidden in the efficiency function $E(v)$ which is local to the crack tip region and independent of the macroscopic regime as will be shown below. The meaning of the efficiency $E(v)$ is as follows: when $E(v)$ is close to zero, the energy delivered to the crack tip is mostly spent in phonon emission so that the mechanism is not sufficient for the crack to advance. When the $E(v)$ is close to one, all the energy delivered is used to break tetrahedra, and the crack can advance promptly. We will see that the dependence on v is crucial in the determination of bands of permitted crack speeds, not described in the continuum elastic theory. The correct derivation of these bands will be given below.

2. *Measuring the energy release rate*

The breakage energy release rate $G_{\rm br}(v,t)$ in our simulations corresponds, for a given crack moving at speed v, to the value of the elastic energy that disappears from the system with each broken tetrahedron at time t. Figure 10 shows measurements from a set of simulations involving samples of of height 120 tetrahedra and up to 3500 tetrahedra long for increasing crack speeds. We observe $G_{\rm br}(v,t)$ to grow linearly with time initially: corresponding measured slopes $G'_{\rm br}(v,0)$ are discussed below. The long crack regime exhibits fluctuations due to waves reflected from the sample boundaries, but the average magnitude $G_{\rm br}(v)$ of the breakage energy release rate can be clearly retrieved.

The $G_{\rm br}(v)$ in the long crack limit is shown as a function of crack speed in figure 11. Vertical lines indicate the speeds at which resonances are expected to be seen according to figure 5. The two lines labelled as α' and β' correspond to resonances due to the dispersion relations of *bulk waves*. Corresponding to each line there is a clear decrease of the energy release rate, meaning that more energy is emitted as radiation.

The crucial feature of figure 11 is that it reveals how the energy available for breaking bonds responds to the speed of the crack, for a given macroscopic energy release rate. This same figure can be read in reverse: given some threshold value for $G_{\rm br}(v)$ corresponding to a given frac-

ture toughness of the material, the possible crack speeds are obtained from the graph.

It can be further argued on grounds of stability that only the speed ranges where $G_{\rm br}(v)$ decreases with v are allowed as steady crack speeds. In the counter case where $G_{\rm br}(v)$ increases with v, a prospective overshoot in v leads to excessive bond breakage energy and hence acceleration, and an undershoot to insufficient breakage energy and the crack must slow further. Thus stable steady crack propagation is confined to narrow intervals associated with resonances and the high speed regime.

It is worth pointing out that most of the features shown in figure 11 are due to high frequency branches either in the first or second Brillouin Zone. The first resonance due to the Rayleigh branch (apart from the resonance at the Rayleigh speed) is the marginally visible ϵ resonance. This shows how important it is to include the full complexity of the band structure within the analysis.

The data in fig. 11 are at constant macroscopic energy release rate G_M^∞, so due to (5.4) they also show the behaviour of the efficiency $E(v)$ with the crack speed. However, if the efficiency $E(v)$ is governed only by local phenomena, then its behaviour with the crack speed should be independent of the crack propagating in steady state or transient regime, provided the crack speed v is fixed. From the knowledge of $E(v)$ then we could find out the dependence of $G_{\rm br}(v,t)$ on the crack speed for any macroscopic set up, provided we know the macroscopic continuum solution.

To verify the independence of $E(v)$ on the dynamic regime, we also analyzed the short crack limit. In this case, the crack can be seen as advancing in an unbounded medium as the sample boundaries are distant from the crack tip. For a planar type-I crack propagating at steady speed v in an unbounded continuum medium the macroscopic transfer of energy to the crack tip (per unit distance advanced) is given by:

$$G_M^0(v,t) = \frac{v^2\alpha_l}{2c_t^2\mu D}K_I^2(v,t). \tag{5.5}$$

Here $\alpha_{t,l} = \sqrt{1-v^2/v_{t,l}^2}$ and $D = 4\alpha_t\alpha_l - (1+\alpha_t^2)^2$. The constants v_l and v_t represent the longitudinal and transverse sound speeds, and $K_I(v,t)$ is the *stress intensity factor* at time t for the given crack speed.

A functional form for $K_I(v,t)$ is available for the Broberg problem[2,21,22] of a crack expanding from zero initial length in a uniform tension field and infinite medium. In particular it can be written in the form:

$$K_I(v,t) = \Sigma(v)\sigma_\infty\sqrt{\pi v t}$$

where σ_∞ is the traction applied on the crack faces. The energy release rate increases linearly with time. As figure 10 shows, we obtain the same behaviour for $G_{\rm br}(v,t)$ in our simulations. In the case of symmetric growth $\Sigma(v)$ has the form:

$$\Sigma(v) = -\frac{I(b/q)R(q)}{b^2 q\sqrt{q^2-a^2}}$$

where $R(q) = (b^2-2q^2)^2 + 4q^2\sqrt{a^2-q^2}\sqrt{b^2-q^2}$ and

$$I^{-1}(b/q) = \frac{q}{b^2}\int_0^\infty \frac{R(i\eta)}{(q^2+\eta^2)^{3/2}\sqrt{a^2+\eta^2}}\,d\eta$$

with $a = v_l^{-1}$, $b = v_t^{-1}$, $q = v^{-1}$. We thus have a closed form for the early time slope $G'_M(v,0)$.

Due to these results, to prove that $E(v)$ is independent of the dynamic conditions we just have to check that

$$E(v,0) = \frac{G'_{\rm br}(v,0)}{G'_M(v,0)} \tag{5.6}$$

matches $E(v)$ already measured from the long crack limit. Simulations of symmetric crack growth can be performed simply by fixing the longitudinal displacement at the left and right boundaries: though this would correspond to having a periodic system of symmetric growing cracks, the interaction between cracks is weak due to the strip geometry. $G'_{\rm br}(v,0)$ then corresponds to the measured slopes of the early regime, and $G'_M(v,0)$ is the time derivative of the macroscopic energy release rate (5.5).

Results of the comparison are reported in table I. Because the product vt corresponds to the crack length, the case $v=0$ was reconstructed by analysing several simulations of static cracks with different crack lengths and retrieving the resulting overall slope. For low and high crack speeds, problems arise when measuring the short crack regime: for low crack speeds data is noisy and there are few points to average; for high crack speeds the long crack limit is achieved soon after the crack starts moving, so that the short crack regime is properly defined only when the sample height is very large with respect to the size of a tetrahedron. This is still not the case even when dealing with our 120 tetrahedra wide sample. Better results for the short crack regime were obtained from simulations of 800×800 tetrahedra as the third column of the table shows.

These results show that the efficiency $E(v)$ is independent of the particular dynamic regime. The absolute values are also of interest. The $v=0$ limit shows that when the tetrahedra at the tip of a static crack are broken, about 75 % of the strain energy released comes from relaxation in other tetrahedra which is radiated in waves. The maximum efficiency (about 60 %) occurs at $v \simeq 0.6\,v_t$. This happens to be just below the Yoffe speed $\sim 0.63\,v_t \simeq 2/3 v_R$, but as our measurements exclude the possibility of crack branching we presume this to be a coincidence.

VI. CONCLUSIONS

We have presented a new finite element model for linear elastic fracture mechanics, which has proved surprisingly and revealingly rich in its behaviour even in the two dimensional case. The model was designed to enable fast numerical simulations of large systems particularly

v/v_t	$2l = 120$ $E(v,0) = \frac{G'_{\rm br}(v,0)}{G'_M(v,0)}$	$2l = 800$ $E(v,0) = \frac{G'_{\rm br}(v,0)}{G'_M(v,0)}$	$2l = 120$ $E(v) = \frac{G^{\infty}_{\rm br}(v)}{G^{\infty}_M(v)}$	$E(v,0)/E(v)$
0.0	0.257 ± 0.006	-	0.2591 ± 0.0008	-
0.1	0.19 ± 0.04	0.22 ± 0.04	0.2408 ± 0.0004	0.9 ± 0.2
0.2	0.52 ± 0.03	0.52 ± 0.01	0.528 ± 0.003	0.98 ± 0.02
0.3	0.40 ± 0.02	0.390 ± 0.006	0.379 ± 0.001	1.03 ± 0.02
0.4	0.44 ± 0.02	0.432 ± 0.004	0.4315 ± 0.0002	1.00 ± 0.01
0.5	0.48 ± 0.02	0.462 ± 0.004	0.4636 ± 0.0001	0.997 ± 0.009
0.6	0.59 ± 0.02	0.576 ± 0.006	0.5767 ± 0.0004	1.00 ± 0.01
0.7	0.55 ± 0.04	0.514 ± 0.006	0.5201 ± 0.0001	0.99 ± 0.01
0.8	0.2 ± 0.1	0.33 ± 0.02	0.3202 ± 0.0001	1.03 ± 0.06
0.9	-	0.079 ± 0.007	0.0890 ± 0.0005	0.89 ± 0.08

TABLE I: The efficiency of energy delivery into bond breaking, compared between the different dynamical regimes of short and long cracks, as a function of crack speed. The second and third columns show the efficiency computed from early time slopes of the energy into bond breakage compared to that macroscopically delivered, for two different sample heights. Results for $v = 0$ were obtained from a set of simulations of static fracture with different notch lengths. Results for low and high crack speeds are influenced by problems in the measurements in the short crack limit: this effect is reduced increasing the size of the sample as shown in the third column. The final column shows the ratio of these short crack regime efficiencies to those computed from the long crack regime shown in the fourth column: these results clearly confirm that the efficiency is insensitive to dynamical regime, consistent with our assertion that it is a property local to the crack tip.

with three dimensions in mind, but the main strengths which we have exploited in this paper are direct control of the local physics which it offers, combined with bulk and surface dispersion relations amenable to simple theoretical computation. Our results suggest that inclusion of known phonon dispersion can be crucial to understanding the speed of fracture propagation.

Our results relate to ideally brittle materials, in that we have included no significant mechanism of local dissipation and most particularly no plastic deformation mechanism. Linear damping is readily included, and indeed could be exploited to mitigate the effects of waves reflected back from the sample edges. Spontaneous crack roughness and branching will be addressed in a following paper.

The crucial mechanism which our results incorporate beyond continuum fracture mechanics is the radiation of phonons from the crack tip. This we show leads to a significant speed dependence in the fraction of macroscopic strain energy available as work to create new surface. For a static crack in our model, this efficiency is only 25 %, thus modifying the most naïve Griffith criterion for crack propagation by a factor of 4. The general rise in bond breaking efficiency with speed towards a global maximum for typical fast crack speeds rules out steady crack propagation at most lower speeds, and remains to be understood more quantitatively.

We have been able to interpret fine structure in the bond breaking efficiency associated with resonant conditions for surface wave emission. This leads to islands of stable crack velocity, which can only arise at lower speeds due to dispersion and hence due to the discrete properties of matter.

A related explanation of the presence of sets of forbidden crack speeds has already been given by M. Marder *et al.*[3,4,5] by using a mechanistic description of bond breakage in terms of most stretched ones. According to this approach cracks cannot advance at speeds below some threshold, since due to lattice oscillations bonds would break before the expected time compatible with the crack speed. A velocity gap then appears. The two approaches seem to be very close indeed, since simulations from Murder *et al.* are based on periodic lattices which should show characteristic dispersion relations. The oscillations between neighbouring sites which stretch the bonds beyond the critical length correspond to wave vectors at the border of the Brillouin zone and ideally should be connected to the presence of resonances towards the zone boundary. Our description however appears to be more general as it expresses the same phenomenon in terms of the energy release rate and phonon band structure. The existence of velocity gaps is shown on the basis of energetic arguments. This has the advantage of not being built up on the particular rule for breaking bonds, but relates the existence of velocity gaps and constant speed advance to a more general description of the properties of the material. Furthermore, velocity gaps can be read directly from the dependence of the strain energy release rate on the crack speed, a relationship which we might eventually hope to deduce or calculate for real materials.

Acknowledgments

AP would like to thank A.Petri for its observations and the useful discussions. We aknowledge support of EU contract n. ERBFMRXCT980183

APPENDIX A: DISPERSION RELATIONS FOR BULK WAVES

We need to find the eigenvalues for eq. (2.9). By inspection $\mathbf{u_k} = \nabla \wedge \nabla^*$ is an eigenvector with eigenvalue

$$\mathrm{A}_{\mathbf{k}} \equiv \frac{\mu\,\Omega'}{m}[\nabla\cdot\nabla^* + \nabla^*\cdot\nabla]. \tag{A1}$$

The remaining two eigenvectors are given by a linear combination of ∇ and ∇^*. We then obtain:

$$\omega^2(b\nabla + c\nabla^*) = \mathrm{A}_{\mathbf{k}}(b\nabla + c\nabla^*) + \\ +\frac{(\lambda+\mu)\,\Omega'}{m}[\nabla\nabla^* + \nabla^*\nabla]\cdot(b\nabla + c\nabla^*). \tag{A2}$$

We can now multiply eq. (A2) by ∇ to the left and by ∇^* to the right, so as to obtain the following coupled equations:

$$\begin{cases} (\epsilon-1)[b\eta + c] &= \beta[2b\eta + c(1+|\eta|^2)] \\ (\epsilon-1)[b + c\eta^*] &= \beta[b(1+|\eta|^2) + 2c\eta^*] \end{cases}$$

with: $\epsilon \equiv \omega^2/\mathrm{A}_{\mathbf{k}}$, $\beta \equiv (\lambda+\mu)\,\Omega'\,\nabla\cdot\nabla^*/(m\,\mathrm{A}_{\mathbf{k}})$ and $\eta \equiv (\nabla\cdot\nabla)/(\nabla\cdot\nabla^*)$. Solving for eigenvalues leads to:

$$\epsilon = 1 + \beta(1 \pm |\eta|) \qquad \text{with} \quad |\eta| \neq \mp 1$$

and substituting back into the equation we obtain:

$$\omega^2 = \mathrm{A}_{\mathbf{k}} + \frac{(\lambda+\mu)\,\Omega'}{m}\Big[(\nabla\cdot\nabla^*) \pm |\nabla\cdot\nabla|\Big] \tag{A3}$$

which together with (A1) completes the dispersion relations.

Having obtained these eigenvalues, it is not difficult to find that the corresponding eigenvectors have the form:

$$\mathbf{u} = \nabla \pm \frac{\nabla\cdot\nabla}{|\nabla\cdot\nabla|}\nabla^*. \tag{A4}$$

APPENDIX B: ADDING DISSIPATION

There are at least two pratical reasons to add dissipation in the dynamics. First, the starting point of any simulation should be a sample in equilibrium: this can be easily obtained by relaxing the lattice to a configuration of minimum energy. The second reason is the possibility to damp out waves that would otherwise propagate and reflect back from the sample borders.

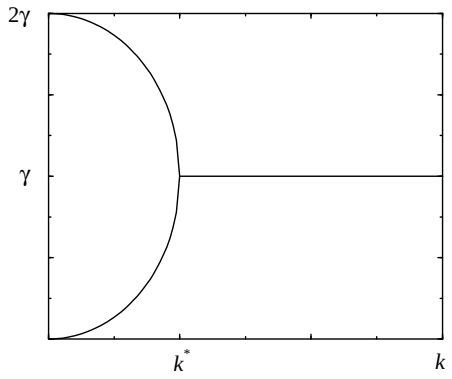

FIG. 12: Damping rate for different values of γ. Note that for $k > k^*$ all modes are damped at the same rate $q = \gamma$.

The physical way to introduce dissipation in the model for linear elasticity is the introduction of a viscosity term in (2.7). However this gives wide dispersion in the damping rates of different modes making it inefficient at relaxing solutions or reducing boundary reflections.

There is a less physical way to obtain dissipation that has the advantage of being less wave vector dependent and simpler to implement. Starting from eq. (2.9) a dissipative term is added so that:

$$m\ddot{\mathbf{u}} + 2m\gamma\dot{\mathbf{u}} + \mathrm{G}(\mathbf{k})\mathbf{u} = 0 \tag{B1}$$

where:

$$\mathrm{G}(\mathbf{k})\mathbf{u} = \Omega'\Bigg\{ -\mu\Big[\nabla\cdot\nabla^* + \nabla^*\cdot\nabla\Big]\mathbf{u} + \\ -(\lambda+\mu)\Big[\nabla\nabla^* + \nabla^*\nabla\Big]\cdot\mathbf{u}\Bigg\}.$$

This approach is clearly unphysical, but useful to reach the configuration of minimal energy or to damp out unwanted reflected waves.

Solutions of the form $\mathbf{u}(t) = e^{-qt}\mathbf{u_k}$ can be found by substitution in (B1), giving $q^2 - 2\gamma q + \mathrm{G}(\mathbf{k})/m = 0$, and leading to

$$\mathrm{Re}\{q\} \;=\; \mathrm{Re}\left\{\gamma \pm \sqrt{\gamma^2 - \left[\frac{\mathrm{G}(\mathbf{k})}{m}\right]}\right\} =$$

$$= \begin{cases} \gamma & \dfrac{\mathrm{G}(\mathbf{k})}{m} \;\geq\; \gamma^2 \\ \begin{cases} 2\gamma - \frac{1}{2\gamma}\left[\dfrac{\mathrm{G}(\mathbf{k})}{m}\right] & \text{fast} \\ & \text{modes} \end{cases} & \dfrac{\mathrm{G}(\mathbf{k})}{m} \;\ll\; \gamma^2 \\ \begin{cases} \frac{1}{2\gamma}\left[\dfrac{\mathrm{G}(\mathbf{k})}{m}\right] & \text{slow} \\ & \text{modes.} \end{cases} & \end{cases}$$

In fig. 12 the damping rate $\mathrm{Re}\{q\}$ is plotted as a function of $|\mathbf{k}|$. Curves depend on the value of the dissipative parameter γ: in particular, the value $k^*(\gamma)$ separates two regimes. For $k > k^*$ all the modes are damped with a damping constant $q = \gamma$, whereas for $k < k^*$ fast and slow modes are damped with different magnitudes. The optimal value for γ is then set by maximising the damping rate of the slowest mode, leading us to set $k^* \equiv k_{\min} = \frac{\pi}{L}$, where L is the size of the lattice in fcc unit cells. The choice is also interesting in that it sets all modes to have the same damping rate

$$\gamma = c_t \frac{\pi}{L}. \tag{B2}$$

The time needed to reduce the potential energy of a factor ϵ towards its minimum is then given by:

$$\Delta t = -\frac{h}{2\pi c_t} \ln \epsilon. \tag{B3}$$

During the dynamics, reflected waves travel a distance of at least L fcc unit cells in a time interval of $\Delta t = L/c_t$, hence when reflected waves reach the crack tip, using the optimal value for γ their intensity is reduced at least by a factor $e^{2\gamma \Delta t} = e^{2\pi} \sim 500$ for transverse waves, and $e^{2\pi \frac{c_t}{c_l}} \sim 25$ for longitudinal waves, using values as in figure 2. Note however that for the results presented in this paper we turned all damping off after initial equilibration.

APPENDIX C: DISPERSION RELATIONS FOR SURFACE WAVES

Consider a solid occupying the portion of space defined by $y < 0$ with the surface $y = 0$ as its only boundary. In the continuum case, surface modes are solutions of $\omega^2 \mathbf{u_k} + \nabla \cdot \overleftrightarrow{\sigma} = 0$ constrained by the boundary condition $\overleftrightarrow{\sigma} \cdot \mathbf{n} = 0$ where $\mathbf{n}$ is the normal to the surface. They consist of linear combinations of bulk waves with different complex k_y (that accounts for their damping towards the interior of the sample) obeying the bulk waves dispersion relations and common ω, k_x and k_z.

We can apply the same principles to our discrete model considering that the layer of sites corresponding to the $y = 0$ plane has no force acting on it from above. It follows therefore:

$$\nabla_1^+ \cdot \overleftrightarrow{\sigma}_2 + \nabla_2^+ \cdot \overleftrightarrow{\sigma}_1 = 0 \tag{C1}$$

where:

$$\begin{cases} \nabla_1^+ &= \displaystyle\sum_{\{v | r_{v,y} > 0\}} \mathbf{r}_v \exp^{i\mathbf{q}\cdot\mathbf{r}_v} \\ \nabla_1^- &= \displaystyle\sum_{\{v | r_{v,y} < 0\}} \mathbf{r}_v \exp^{i\mathbf{q}\cdot\mathbf{r}_v} \\ \nabla_1 &= \nabla_1^+ + \nabla_1^-. \end{cases}$$

Hence:

$$\nabla^+(\mathbf{k}) \equiv \nabla_1^+(\mathbf{k}) = -\nabla_2^-(-\mathbf{k}).$$

Using eq. (2.8), the boundary condition (C1) becomes:

$$\mathrm{B}(\mathbf{k})\mathbf{u} = \lambda(\nabla_2^+ \cdot \nabla_1 + \nabla_1^+ \cdot \nabla_2)\mathbf{u} +$$

$$\lambda(\nabla_1 \nabla_2^+ + \nabla_2 \nabla_1^+) \cdot \mathbf{u} + \mu(\nabla_2^+ \nabla_1 + \nabla_1^+ \nabla_2) \cdot \mathbf{u} = 0.$$

We can solve this equation by expressing $\mathbf{u}$ as a linear combination of bulk eigenvectors $\mathbf{u} = a\mathbf{e}_1 + b\mathbf{e}_2 + c\mathbf{e}_3$ with common ω, k_x and k_z. For simplicity we can reduce to the case[23] $k_z = 0$.

Bulk dispersion relations for $k_z = 0$ have therefore the form $\omega = f_\alpha(k_x, k_y)$. These can be inverted such that $k_y = f_\alpha^{-1}(\omega, k_x)$. Hence, surface modes are solutions of the following equation:

$$\det \begin{pmatrix} \Big(\mathrm{B}(\mathbf{k})\mathbf{e}_1\Big)_{k_y \to f_1^{-1}(\omega,k_x)} \\ \Big(\mathrm{B}(\mathbf{k})\mathbf{e}_2\Big)_{k_y \to f_2^{-1}(\omega,k_x)} \\ \Big(\mathrm{B}(\mathbf{k})\mathbf{e}_3\Big)_{k_y \to f_3^{-1}(\omega,k_x)} \end{pmatrix} = 0$$

provided $\mathrm{Im}\{f_1^{-1}(\omega, k_x), f_2^{-1}(\omega, k_x), f_3^{-1}(\omega, k_x)\} > 0$.

[1] L. D. Landau and E. M. Lifshitz, *Theory of Elasticity* (Pergamon Press, London, 1959)
[2] L. B. Freund, *Dynamic Fracture Mechanics* (Cambridge University Press, 1990)
[3] M. Marder and S. Gross, J. Mech. Phys. Solids **43**, 1 (1995)
[4] D. Holland and M. Marder, Advan. Mater. **11**, 793 (1999)
[5] J. Fineberg and M.Marder, Phys. Rep. **313**, 2 (1999)
[6] K. E. Bullen, *Seismology*, (Methuen & co, London, 1954)
[7] D. S. Parasnis, *Principles of applied geophysics*, (Methuen & co, London, 1962)
[8] F. F. Abraham, D. Brodbeck, R. A. Rafey and W. E. Rudge Phys. Rev. Letters **73**, 272 (1994)
[9] S. J. Zhou, D. M. Beazley, P. S. Lomdahl and B. L. Holian, Phys. Rev. Lett. **78**, 479 (1997)
[10] D. Holland and M. Marder, Phys. Rev. Lett. **80**, 746 (1998)
[11] O. Pla, F. Guinea, E. Louis, S. V. Ghaisas and L. M. Sander, Phys. Rev. B **57**, R13981 (1998)
[12] O. Pla, F. Guinea, E. Louis, S. V. Ghaisas and L. M. Sander, Phys. Rev. B **61**, 11472 (2000)
[13] T. Martín, P. Español, M. A. Rubio and I. Zúñiga Phys.

Rev. E **61**, 6120 (2000)
[14] G. Caldarelli, R. Cafiero and A. Gabrielli, Phys. Rev. E **57**, 3878 (1998)
[15] S. J. D. Cox and L. Paterson, Phys. Rev. B **40**, 4690 (1989)
[16] E. Johnson, Int. J. Fract. **55**, 47 (1992)
[17] X. -P. Xu and A. Needleman, J. Mech. Phys. Solids **42**, 1397 (1994)
[18] F. Nilsson, Dynamic stress-intensity factors for finite strip problems, Int. J. Fract. **8**, 403 (1972)
[19] M. P. Allen, D. J. Tildeslay, *Computer simulation for liquids*, (Clarendon Press, Oxford, 1987)
[20] D. Franken, B. Smit, *Understanding molecular simulation*, (Academic Press, 2002) pp 77-81
[21] K. B. Broberg, Archiv för Fysic **18**, 159 (1960)
[22] K. B. Broberg, *Cracks and fracture*, (Academic Press, 1999)
[23] We are interested in particular to the <100> direction, however the more general case can be obtained by following the same steps.